

# Efficient Generation of Extreme Ultraviolet Light From Nd:YAG-Driven Microdroplet-Tin Plasma

R. Schupp,<sup>1</sup> F. Torretti,<sup>1,2</sup> R.A. Meijer,<sup>1,2</sup> M. Bayraktar,<sup>3</sup> J. Scheers,<sup>1,2</sup> D. Kurilovich,<sup>1,2</sup> A. Bayerle,<sup>1</sup> K.S.E. Eikema,<sup>1,2</sup> S. Witte,<sup>1,2</sup> W. Ubachs,<sup>1,2</sup> R. Hoekstra,<sup>1,4</sup> and O.O. Versolato<sup>1,\*</sup>

<sup>1</sup>*Advanced Research Center for Nanolithography, Science Park 106, 1098 XG Amsterdam, Netherlands*

<sup>2</sup>*Department of Physics and Astronomy and LaserLaB, Vrije Universiteit, De Boelelaan 1081, 1081 HV Amsterdam, Netherlands*

<sup>3</sup>*Industrial Focus Group XUV Optics, MESA+ Institute for Nanotechnology, University of Twente, Drienerlolaan 5, 7522 NB Enschede, Netherlands*

<sup>4</sup>*Zernike Institute for Advanced Materials, University of Groningen, Nijenborgh 4, 9747 AG Groningen, Netherlands*



(Received 18 December 2018; revised manuscript received 20 February 2019; published 8 July 2019)

We experimentally investigate the emission of EUV light from a mass-limited laser-produced plasma over a wide parameter range by varying the diameter of the targeted tin microdroplets and the pulse duration and energy of the 1- $\mu\text{m}$ -wavelength Nd:YAG drive laser. Combining spectroscopic data with absolute measurements of the emission into the 2% bandwidth around 13.5 nm relevant for nanolithographic applications, the plasma's efficiency in radiating EUV light is quantified. All observed dependencies of this radiative efficiency on the experimental parameters are successfully captured in a geometrical model featuring the plasma absorption length as the primary parameter. It is found that laser intensity is the pertinent parameter setting the plasma temperature and the tin-ion charge-state distribution when varying laser pulse energy and duration over almost 2 orders of magnitude. These insights enabled us to obtain a record-high 3.2% conversion efficiency of laser light into 13.5-nm radiation and to identify paths towards obtaining even higher efficiencies with 1- $\mu\text{m}$  solid-state lasers that may rival those of current state-of-the-art CO<sub>2</sub>-laser-driven sources.

DOI: [10.1103/PhysRevApplied.12.014010](https://doi.org/10.1103/PhysRevApplied.12.014010)

## I. INTRODUCTION

Highly charged tin ions in laser-produced transient plasmas are the atomic sources of EUV light at 13.5-nm wavelength for nanolithography [1–15]. In state-of-the-art EUV sources such plasmas are produced by irradiation of micrometer-sized tin droplets with high-power CO<sub>2</sub>-gas-laser pulses [16–18] in a two-step process where first a laser prepulse [16–23] shapes the droplet into a target optimized for EUV production with a second, more energetic pulse. Key physical processes were reviewed by Banine *et al.* [14].

Alternatively, solid-state 1- $\mu\text{m}$ -wavelength Nd:YAG laser systems can be used for plasma creation, offering significant advantages over the 10- $\mu\text{m}$ -wavelength CO<sub>2</sub> drive laser. The advantages include an improved energy efficiency, a significantly more compact size at the same output power and improved temporal pulse-shaping capabilities. Moreover, they could enable a single-pulse irradiation scheme. YAG systems may, in fact, replace CO<sub>2</sub>

lasers if the efficiency of converting laser energy into radiation within a 2% bandwidth around 13.5 nm that can be reflected by multilayer optics [24,25] gets sufficiently competitive.

Nd:YAG-driven light sources have a much higher, near complete laser absorptivity due to the strong increase of the critical plasma electron density  $n_c$  with decreasing wavelength  $\lambda$  ( $n_c \propto \lambda^{-2}$ ). The cross section of the here dominant [26] inverse bremsstrahlung absorption mechanism strongly increases with electron density [27,28]. However, the density increase may cause self-absorption of the emitted EUV light, leading to opacity-broadened emission [29–32]. In turn, more light is emitted outside of the accepted bandwidth. Modeling these opacity effects challenges even the most advanced atomic structure calculations [12] due to the strongly correlated electronic structure of the multielectron open-4d-shell tin ions raising the need for experimental investigations.

The literature on Nd:YAG-driven tin plasma mostly deals with the emission from planar solid targets [31–42], tin-coated spherical targets [29,43–47], or liquid-droplet targets out of tin alloys [48]. The literature covering

\*o.versolato@arcn.nl

the emission properties of laser-produced plasma (LPP) from high-purity tin microdroplets, the industrial targets of choice, remains scarce [49–51].

Here, we present the results of a systematic investigation of the characteristics of the EUV spectra of these sources over a wide parameter range, varying the diameter of the targeted, pure tin microdroplets (16–65  $\mu\text{m}$ ), the laser pulse duration (0.5–25 ns) and its energy, presented as intensity  $[(0.1\text{--}2.7) \times 10^{11} \text{ W/cm}^2]$ , using a transmission-grating spectrometer [52,53]. The combination of this spectroscopic data with absolute measurements of the *in-band* emission in the 2% bandwidth around 13.5 nm enables three linked figures of merit to be obtained characterizing the emission from the plasma: spectral purity, conversion efficiency, and radiative efficiency. Conversion efficiency (CE) is commonly used and represents the ratio of  $E_{\text{IB},2\pi}$  over the energy of the drive laser ( $E_{\text{laser}}$ ).  $E_{\text{IB},2\pi}$  is the total in-band radiation emitted into the half sphere back towards the laser that is reflected by the light collection optics in industrial sources. Spectral purity (SP) is defined as the ratio of  $E_{\text{IB},2\pi}$  and total EUV energy ( $E_{\text{rad},2\pi}$ ) emitted in the same half sphere. Through basic energy-conservation considerations, SP serves as an absolute upper limit to the conversion efficiency:  $\text{CE} \leq \text{SP}$ , where CE approaches SP only in the case of light emission solely in the backward-facing half sphere. This limit value is lowered by considering that light is also emitted in the opposite, forward-facing half sphere. Indeed, a more stringent limit of  $\text{CE} \leq \text{SP}/2$  holds in the case of spherically symmetric emission [54]. These limits emphasize the importance of spectroscopic investigations as introduced here.

Considering the application purposes, the radiative efficiency  $\eta_{\text{rad}}$  is defined as the ratio of  $E_{\text{rad},2\pi}$  to laser energy  $E_{\text{laser}}$  and it thus equals the ratio CE/SP. Simulation works predict that in total 70% up to 90% of the absorbed laser light is emitted as radiation [55–57]. For optimal, high-CE source operation both SP and radiative efficiency should be as high as possible. A further crucial requirement is that the plasma should create manageable amounts of debris comprising, e.g., fragments or high-energy particles that could limit the optics lifetime. Laser energy not contributing to radiation may instead contribute to generating fast ionic debris. Possible gains in radiative output power should be carefully measured out against, e.g., increases in the material load on the optical components. A full quantification of various debris loads is left for future work.

In order to optimize the three figures of merit of EUV-source operation, we introduce a geometrical model with the plasma-absorption length as its prime parameter. The model describes very well the dependencies of  $\eta_{\text{rad}}$  on source parameters such as droplet size and laser-beam size. Employing these insights, we obtain a record-high CE of 3.2% and identify paths towards even higher values.

This paper is structured as follows. In Sec. II the experimental setup is introduced, followed by a description of the measurements in Sec. III. A plasma expansion model is presented in Sec. IV that is applied to the experimental data in Sec. V. In Sec. VI we apply the found scalings to an industrially relevant case and close with a discussion of our findings in Sec. VII.

## II. EXPERIMENTAL SETUP

Molten Sn of 99.995% purity is pushed through a capillary glass tube with a micrometer-sized orifice into a vacuum chamber of  $5 \times 10^{-7}$  mbar background pressure. Plateau-Rayleigh instabilities lead to the breakup of the liquid stream into small fragment droplets. Evenly sized microdroplets are produced from these fragments by inducing a pressure modulation on the liquid stream in the glass tube leading to a controlled coalescence of the smaller fragment droplets. The resulting microdroplet size, measured using imaging techniques [19,55], is controlled by variation of the applied modulation frequency. Modulation frequencies between 3 and 100 kHz are used resulting in droplets between 65 and 20  $\mu\text{m}$  in diameter. Above 100 kHz the interdroplet spacing is on the order of the laser-beam spot size; therefore, in order to produce droplets as small as 16  $\mu\text{m}$  with sufficient spacing, we make use of imperfect coalescence resulting in periodic groups of smaller and bigger droplets.

The droplets travel at 10 m/s through a He-Ne laser light sheet scattering the laser light, which is subsequently detected by a photomultiplier tube and used to trigger the drive laser and the data-acquisition system at 10 Hz. After detection, the droplet is irradiated by a linearly polarized, high-intensity laser pulse from an in-house built Nd:YAG laser system seeded at 1064 nm [58]. The laser system produces a flat-top spatial profile and has temporal pulse-shaping capabilities allowing the production of pulses from 0.4 to 1000 ns duration. All but the 0.5-ns pulse are box shaped and their duration is measured as FWHM.

With the purpose of maintaining the homogeneous spatial intensity distribution, the laser beam is imaged from the exit of the amplifier rod onto the droplet. In order to match droplet and laser-beam spot size, and to reach the necessary intensities on the order of  $10^{11} \text{ W/cm}^2$ , the laser beam is demagnified to 96  $\mu\text{m}$  FWHM. Of the total laser pulse energy, a fraction of 80% falls within the FWHM area. To obtain an even smaller beam spot size of 56  $\mu\text{m}$ , used for measurements described in Sec. VI, a 3.5-mm aperture is placed in the object plane of the beam. In both cases, the laser-beam spot is slightly elliptical, with less than 25% difference between the major and minor axis, and we use the average value of the two axes. The laser-beam energy is controlled using a combination of a half-wave plate and a thin-film polarizer without affecting the spatial intensity distribution.

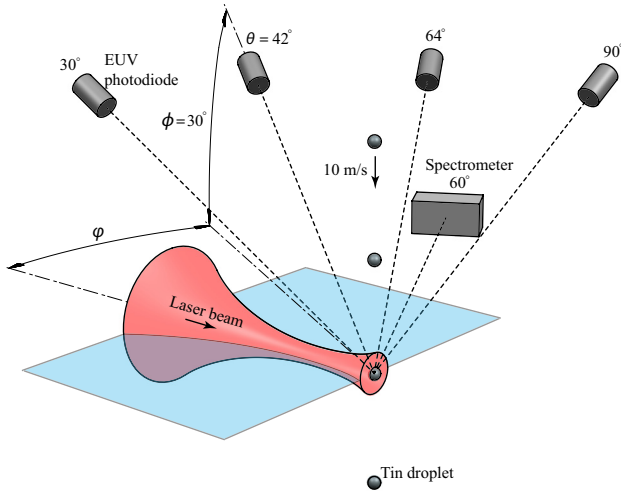


FIG. 1. Schematic representation of the experimental setup. The laser beam, depicted in red, illuminates the falling tin microdroplets (gray spheres). The produced plasma emission is observed using a transmission-grating spectrometer (gray box) as well as four EUV photodiode assemblies (gray cylinders) measuring the absolute amount of produced in-band radiation. All angles  $\theta$  are indicated with respect to the laser-beam propagation axis, with  $\cos \theta = \cos \phi \cos \varphi$ .

The spectral emission of the produced plasma is observed under an angle of  $60^\circ$  (see Fig. 1) using a broadband transmission-grating spectrometer [52,53]. The spectrometer is operated with an entrance-slit width of  $25 \mu\text{m}$  and a 10 000 lines/mm grating obtaining an instrument resolution of 0.1 nm FWHM at 13 nm [52]. The dispersed light is captured by a back-illuminated CCD from Greateyes (GE2048 512BI UV1), cooled to  $-30^\circ\text{C}$  to reduce thermal noise.

The measured images are cropped and corrected for shear and tilt introduced by a slight misalignment of slit and grating with respect to the camera pixel array. Afterwards the images are averaged over the nondispersive axes and the read-out noise and dark counts are eliminated by subtracting a dark exposure image (i.e., an image obtained using the same exposure time but without plasma present). Calibration of the dispersive axis is performed using reference spectra entailing tabulated [59], well-known  $\text{Al}^{3+}$  and  $\text{Al}^{4+}$  line features between 11 and 16 nm. The calibration spectra are taken after the experiments by irradiating a solid aluminum target with the Nd:YAG laser at the same position as the droplets. After calibration, the spectra are corrected for second-order contributions in the wavelength range above 11 nm using the second-order diffraction efficiency of the grating [53]. Lastly, the spectra are divided by the first-order diffraction efficiency of the grating as well as the quantum efficiency of the camera. Since the grating transmission is not calibrated below 5.5 nm, all SP values in the following are calculated for a

wavelength range of 5.5–25.5 nm. Given the low-emission anisotropies observed over the backward half sphere (see below), spectra obtained under an angle of  $60^\circ$  are used for SP.

To obtain an absolute measurement of the produced in-band radiation ( $13.5 \text{ nm} \pm 1\%$ ), four silicon photodiode assemblies are mounted under angles of  $30^\circ$ ,  $42^\circ$ ,  $64^\circ$ , and  $90^\circ$  (Fig. 1). Photodiode measurements are corrected for their respective solid-angle coverage. These assemblies use Mo/Si multilayer mirrors (MLMs) [24,25] as found in industrial sources to reflect the in-band part of the radiation onto the photodiodes. Any remaining optical light reflected by the MLMs is subsequently removed by a Si/Zr coating on the photodiodes (SXUV100), which is transmissive for in-band radiation. The response function of all individual components is known, providing a measure of the absolute amount of produced in-band radiation.

In order to take into account the emission anisotropy over the backward half sphere where CE is defined, we integrate the angular dependency  $f(\theta)$  of the in-band emission. For integration the obtained measurements from the photodiodes in Fig. 2 are used, employing the cylindrical symmetry of the system with respect to the laser beam axis,

$$\text{CE} \propto \int_0^{\pi/2} d\theta f(\theta) \sin(\theta), \quad (1)$$

where the angular dependence  $f(\theta)$  of the in-band emission is typically described by (e.g., Refs. [37] and [60])

$$f(\theta) = \alpha + \beta \cos^{\gamma}(\theta). \quad (2)$$

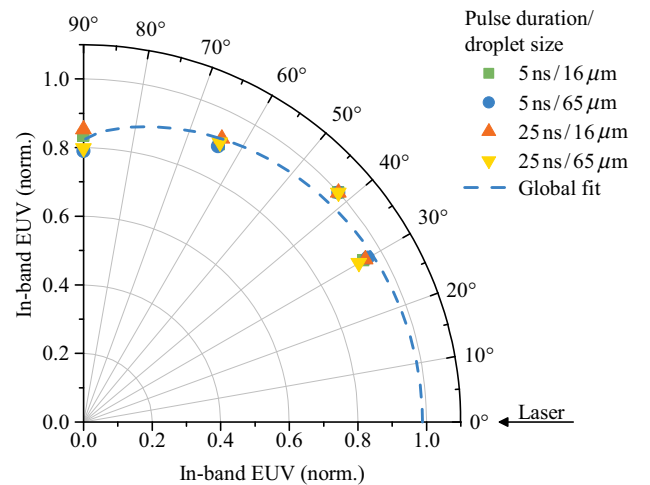


FIG. 2. Angular dependency ( $\theta$ ) of the in-band emission with respect to the laser-beam axis. Depicted are measurements for the  $96\text{-}\mu\text{m}$  laser-beam size. For each pulse duration, the data from the smallest and biggest droplet sizes are shown normalized to their maximum values. The dashed blue line is the result of a global fit of Eq. (2).

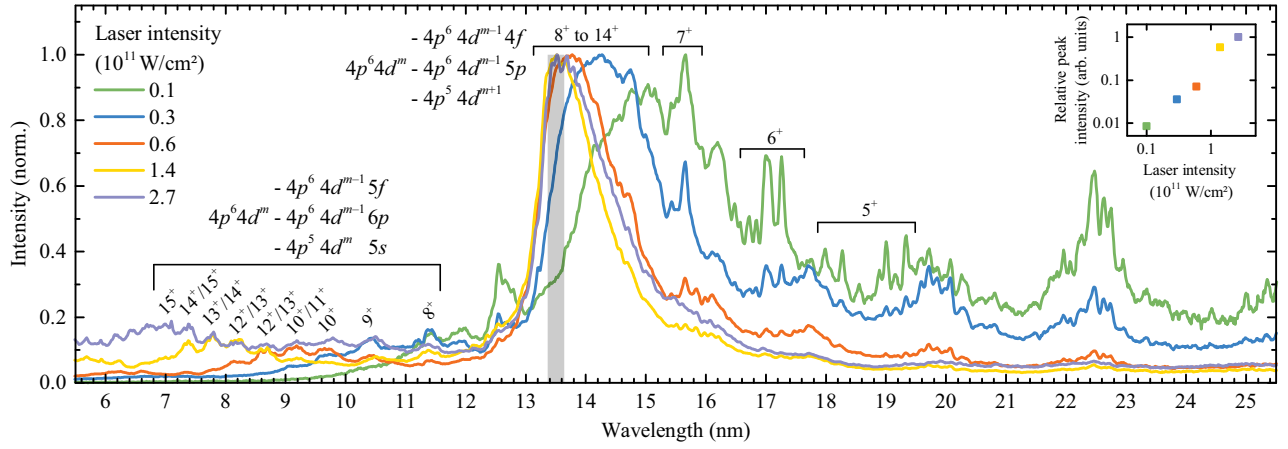


FIG. 3. Normalized emission spectra for various Nd:YAG laser intensities resulting from a 46- $\mu\text{m}$ -diameter tin droplet illuminated with a 96- $\mu\text{m}$ -sized laser beam of 15-ns duration. The gray-shaded area shows the 2% bandwidth around 13.5 nm, relevant for nanolithographic applications. The emission features attributed to the various Sn ions are labeled with the respective charge-state number. Also labeled are the most relevant transition arrays contributing to the in-band emission and the short-wavelength features between 7 and 12 nm, where  $m$  is an integer between 0 and 6 corresponding to  $\text{Sn}^{14+}$  and  $\text{Sn}^{8+}$ , respectively [4,6,61]. The inset figure shows the relative peak-emission intensities as a function of laser pulse intensity.

Fitting Eq. (2) to the measured data, we obtain the following values for the fit parameters:  $\alpha = 0.82(2)$ ,  $\beta = 0.17(3)$ , and  $\gamma = 0.6(3)$ . From integration we obtain a value for the anisotropy-corrected CE that is only 5% lower than the value from the photodiode under  $30^\circ$  angle that we use throughout this paper, extrapolated assuming isotropic emission.

### III. MEASUREMENT RESULTS

In order to optimize SP and  $\eta_{\text{rad}}$ , and therewith CE, we vary three key parameters of our LPP source: laser intensity (see Fig. 3), laser pulse duration, and droplet size. Following this order, we describe below their impact on the observed spectra and the values of SP and CE as presented in Fig. 4. The trends in the radiative efficiency, defined as  $\eta_{\text{rad}} \equiv \text{CE}/\text{SP}$  are described in Sec. V. It is preceded by the introduction of a plasma expansion model in Sec. IV describing the scaling of  $\eta_{\text{rad}}$ .

#### A. Laser intensity

We start by describing the effect of changing the laser intensity using the example of a 96- $\mu\text{m}$ -sized, 15-ns-long laser-beam pulse and a 46- $\mu\text{m}$ -diameter droplet. The intensity, calculated as  $I = E_{\text{laser}}/(\tau\pi w^2)$  using the laser pulse duration  $\tau$  and laser-beam radius  $w = \text{FWHM}/2$ , is varied over more than 1 order of magnitude in the range of  $(0.1\text{--}2.7) \times 10^{11} \text{ W/cm}^2$  by changing the laser-beam energy. The normalized emission spectra arising from these experimental conditions are shown in Fig. 3 and in reduced size in Fig. 4(a).

The most prominent characteristic observed in Fig. 3 is the shift of the main emission feature from 15 nm

toward the desired 13.5 nm with increasing laser intensity. This shift is related to the creation of tin ions of higher charge states ( $\text{Sn}^{8+}$  to  $\text{Sn}^{15+}$ ) relevant for in-band emission [1,4,6,12]. Additionally, the main emission feature narrows towards higher intensity, reaching a FWHM of 0.9 nm at  $1.4 \times 10^{11} \text{ W/cm}^2$ .

At the lower intensities, characteristic emission from  $\text{Sn}^{5+}$  to  $\text{Sn}^{7+}$  is visible in the long wavelength region (15–25 nm) indicating a suboptimal charge-state distribution for creation of in-band radiation. With increasing intensity these emission features become less prominent. To resolve which charge states are contributing to in-band emission at a given intensity we look at the short-wavelength emission between 7 and 12 nm. As described in Refs. [3] and [61],  $\text{Sn}^{8+}$  to  $\text{Sn}^{15+}$  have unique emission features in this regime stemming from radiative decay out of electronic configurations such as, e.g., the  $4p^5 5s$  in  $\text{Sn}^{14+}$  where a  $4p$  core electron is promoted to the  $5s$  sub-shell. These configuration lie above the in-band contributing  $4p^5 4d^{m+1} + 4p^6 4d^{m-1} 4f + 4p^6 4d^{m-1} 5p$  (cf. Fig. 3). Using such out-of-band features as diagnostics it is evident that for the highest laser intensity ( $2.7 \times 10^{11} \text{ W/cm}^2$ ) charge states of at least up to  $\text{Sn}^{15+}$  are present in the plasma.

The above observations relate to the trend in SP values presented in Fig. 4(d) where we see a sharp increase in SP between 0.1 and  $0.5 \times 10^{11} \text{ W/cm}^2$ . Above  $0.5 \times 10^{11} \text{ W/cm}^2$  the incline in SP slows down and SP levels off in the range of  $(0.8\text{--}1.7) \times 10^{11} \text{ W/cm}^2$  before it decreases again. The sharp increase in SP is explained by an increase in average charge state of the plasma causing reduced emission above 16 nm while favoring in-band emission. At the same time the amount of short wavelength radiation



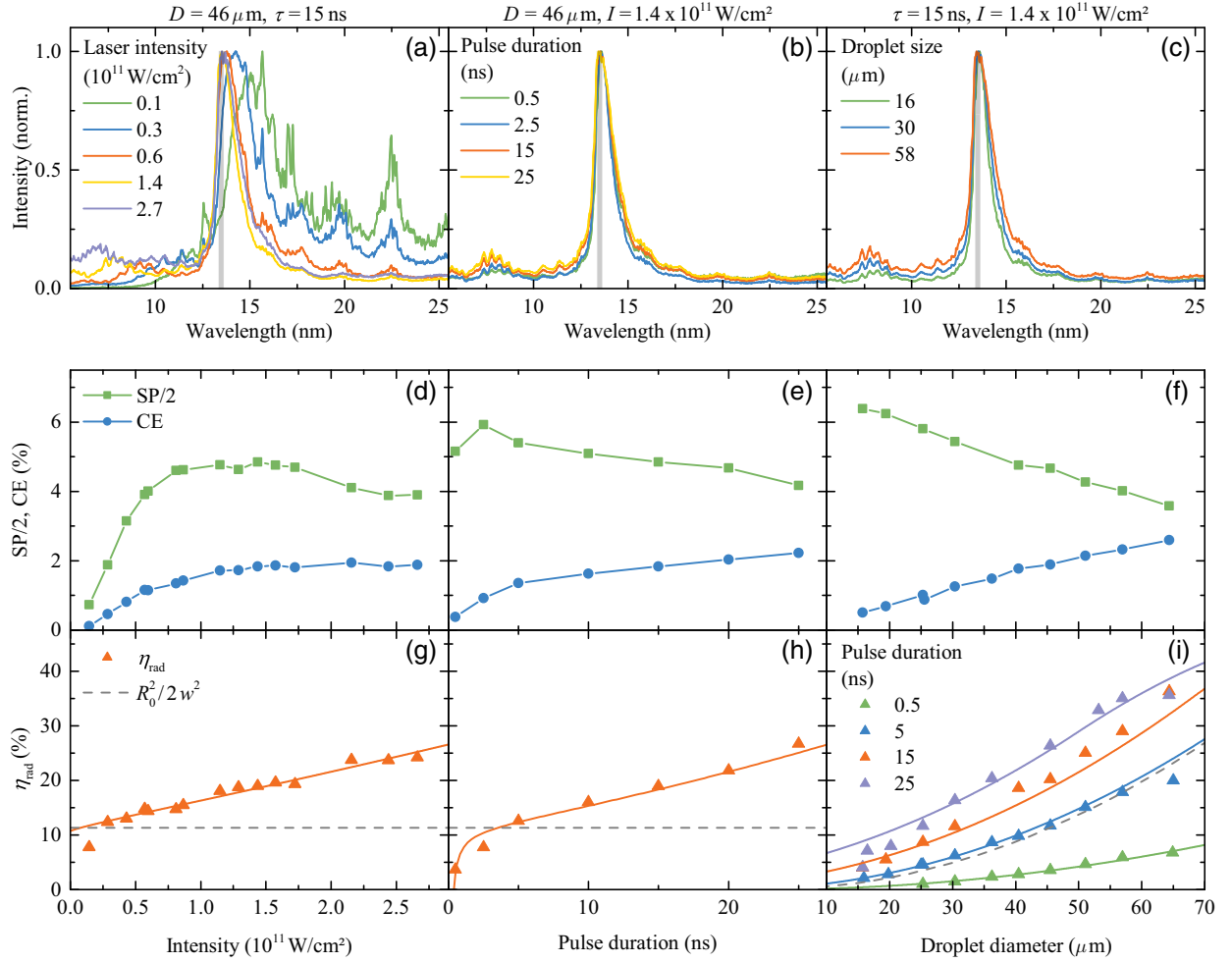


FIG. 4. Top row: spectra for tin microdroplets irradiated by (a) various Nd:YAG laser pulse intensities, (b) laser pulse durations, and (c) droplet sizes. The gray vertical bar depicts a 2% bandwidth around 13.5 nm. Center row: SPs (here divided by a factor 2 for convenience) and CE corresponding to the spectra above. Bottom row: radiative efficiencies ( $\eta_{\text{rad}} \equiv \text{CE}/\text{SP}$ ) and the result of a global fit of our plasma expansion model as described in Sec. V (solid lines). The gray dashed lines in (g)–(i) depict the geometrical overlap ( $R_0^2/2w^2$ ) of laser beam and droplet for isotropic emission.

(below 12 nm) increases steadily. Nevertheless, SP continues rising due to the narrowing of the main spectral feature at 13.5 nm. Above  $1.4 \times 10^{11} \text{ W/cm}^2$  SP declines very slowly because the main emission peak stops narrowing while the amount of short wavelength radiation keeps on increasing. At intensities above  $1.7 \times 10^{11} \text{ W/cm}^2$  the main feature widens again leading to a more rapid decrease of SP. For the lowest and highest intensities measured an increasing fraction of the emission is outside the measured or calibrated range, respectively, slightly increasing the SP.

Even though SP decreases again at higher intensities, CE monotonically increases over the entire intensity range as shown in Fig. 4(d), reaching values up to 1.9%.

### B. Laser pulse duration

In this section we explore the influence of laser pulse duration on the plasma emission as presented in Fig. 4(b).

For the measurements we chose an intensity of  $1.4 \times 10^{11} \text{ W/cm}^2$  at which the main emission feature is narrowest and SP is highest. The droplet diameter as well as the beam size are left unchanged at 46 and 96  $\mu\text{m}$ , respectively.

Upon reducing the laser pulse duration, a narrowing of the main emission peak at 13.5 nm is visible as well as a reduction of the short and long wavelength radiation. The only exception is the pulse duration of 0.5 ns for which the main feature widens again and more emission is observed above 16 nm. For all pulse durations the strong resemblance of the spectra is remarkable indicating that the laser intensity is the pertinent parameter setting the plasma temperature and charge-state distribution. All spectra show similar features and only small differences are visible in the relative emission intensity around 8 nm as well as in the width of the dominant feature at 13.5 nm. The widening of

the main emission feature can be attributed to changes in optical depth of the plasma induced by the different plasma sizes for the various laser pulse durations. The larger optical depth causes increased absorption and re-emission of EUV radiation resulting in the observed broadening of the spectral features.

Translating these observations into the SP curve in Fig. 4(e), we see an increase in SP from 0.5 to 2.5 ns where it reaches its maximum value. Above 2.5 ns a steady but rather weak decrease from 12 to 8% is visible.

As in the preceding subsection, the measured CE monotonically increases with pulse duration. In the scanned parameter range a relatively high CE of 2.2% is reached at 25 ns.

### C. Droplet size

Lastly, we show the effect of a change in droplet diameter onto the spectral emission in Fig. 4(c). For the measurements shown, a pulse duration of 15 ns is used at an intensity of  $1.4 \times 10^{11}$  W/cm<sup>2</sup>. Enlarging the droplet diameter leads to increased relative emission at wavelengths below 13 nm while all spectra show strong similarity with respect to their emission features. Again, predominantly the width of the main emission feature varies and its change can be attributed to changes in the optical depth of the plasma.

Looking at SP in Fig. 4(f), we find a steady decline from 13% at 16  $\mu$ m to 8% at 58  $\mu$ m diameter. Once more, in contrast to the scaling of SP, CE monotonically increases over the entire range of droplet diameters.

## IV. PLASMA EXPANSION MODEL

For all cases presented in Fig. 4, CE increases monotonically with the scanned parameter, even when SP declines. This behavior can be understood as an increase in radiative efficiency that counteracts the losses in SP for bigger droplets and longer pulses. To describe the changes in radiative efficiency with respect to laser intensity, pulse duration, and droplet radius we develop a model taking into account the increase in laser light absorption due to plasma expansion during the laser irradiation.

In the model,  $\eta_{\text{rad}}$  is proportional to the absorbed laser light assuming that a constant fraction is lost to plasma kinetics. At time  $t_0$  when the laser pulse arrives at the droplet the absorbed laser light fraction equals the spatial overlap of droplet and laser beam. At the intensities used, reflectivity can be neglected, resulting in full absorption within the overlap region [55].

The absorbed laser light leads to ablation and plasma creation beyond a certain threshold laser intensity [19,55]. This plasma expands establishing a radial density gradient around the droplet [55] (see Fig. 5). All laser light is absorbed close to an electron density that is of the order

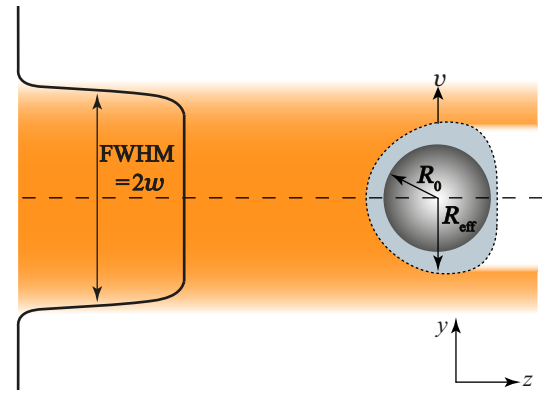


FIG. 5. Schematic representation of the laser-produced plasma system. The laser pulse (orange shaded area) propagating in positive  $z$  direction is absorbed by the liquid Sn droplet of radius  $R_0$  (gray sphere). During laser irradiation plasma is created around the droplet (light gray shaded area) increasing the absorbing area. The latter expands with a constant velocity  $v$  laterally to the laser-beam propagation direction, increasing the effective radius of absorption to  $R_{\text{eff}} = R_0 + vt$ .

of, but below, the critical electron density for the Nd:YAG laser wavelength ( $n_c = 1 \times 10^{21}$  e/cm<sup>3</sup>) [26]. With time, the density contour at which laser light is absorbed moves outwards and the absorptive area increases. Analogously to Refs. [19] and [62], we introduce a power law, here for the lateral expansion speed  $v(I) = a \times I^b$ , at which this density contour moves outwards. The expansion speed is constant over the duration of the laser pulse. Before the plasma can efficiently emit radiation it needs to be heated to reach the relevant plasma temperatures. During this time no significant amount of in-band radiation is emitted implying a lowering of the radiative efficiency. To capture this effect a plasma heat-up time  $t_h$  is introduced as a multiplicative factor  $(1 - t_h/\tau)$  following Ref. [63], where  $\tau$  is the laser pulse duration. To account for the fraction of laser energy lost to plasma kinetics and into radiation emitted towards the forward-facing half sphere, we introduce the maximal radiative efficiency  $\eta_{\text{max}}$ .

Next, we divide the calculation into three cases: (i)  $R_0 + v\tau \leq w$ ; (ii)  $R_0 + v\tau > w$ ; (iii)  $R_0 \geq w$ . In case (i), the droplet is initially smaller than the beam and the absorbing area expands during the laser irradiation, but will not exceed the laser beam size during the pulse. In case (ii), the droplet is smaller than the beam but the absorbing surface exceeds the laser-beam size before the laser pulse ends. In this case we neglect any expansion beyond time  $t_w = (w - R_0)/v$  when the absorbing surface exceeds the laser beam because from thereon full overlap of laser and plasma is reached. In the most extreme case (iii), the liquid droplet itself is already larger than the beam leading to unity absorption during the entire laser

pulse duration. These considerations lead to the following smooth, continuous global fit function:

$$\eta_{\text{rad}} = \left(1 - \frac{t_h}{\tau}\right) \eta_{\text{max}} \quad (3)$$

$$\times \begin{cases} \frac{\frac{1}{3}v^2\tau^3 + R_0v\tau^2 + R_0^2\tau}{w^2\tau}, & \text{(i)} \\ \frac{\frac{1}{3}v^2t_w^3 + R_0vt_w^2 + R_0^2t_w}{w^2\tau} + \frac{\tau - t_w}{\tau}, & \text{(ii)} \\ 1. & \text{(iii)} \end{cases}$$

There are only three main free fit parameters, being  $\eta_{\text{max}}$ ,  $t_h$ , and  $v$ , where the latter is, in turn, composed of two free fit parameters  $a$  and  $b$  (relevant only for the laser-intensity dependency).

## V. MODEL FIT AND DISCUSSION

The obtained radiative efficiencies are presented in Figs. 4(g)–4(i) and our model can be used to understand the monotonous nature of their rise with all varied parameters. The result of a single, *global* fit of our model [see Eq. (3)] to all experimental data related to the variation of the laser pulse duration and droplet diameter is depicted in Figs. 4(h) and 4(i), where all data are taken at a constant intensity of  $1.4 \times 10^{11}$  W/cm<sup>2</sup>. An excellent agreement between model and experiment is obtained. From the fit a plasma expansion velocity  $v = 0.9(1)$   $\mu\text{m}/\text{ns}$ , a maximal radiative efficiency of  $\eta_{\text{max}} = 49(2)\%$  and a plasma heat-up time  $t_h = 0.34(2)$  ns are retrieved. The radiative efficiency from the geometrical laser-droplet overlap, without considering the expanding plasma, is given by  $R_0^2/2w^2$  for isotropic emission shown as dashed lines in Figs. 4(g)–4(i).

The plasma heat-up time  $t_h$  agrees well with the 0.4 ns calculated in Ref. [64] for Nd:YAG-produced Sn plasmas of about 30-eV temperature. However, further transient effects in the plasma due to, e.g., the finite rise and fall times that are a dominant part of the shortest pulse, cannot be excluded. Given its small, sub-ns value,  $t_h$  has negligible impact on radiative efficiency except for the shortest, 0.5-ns pulse-duration case.

The fitted value of the maximal radiative efficiency of 49% (with a highest experimentally obtained value of approximately 35%) comes close to the maximally possible value of 50% in the case of isotropic emission. As energy is invariably lost through other processes such as ionization and plasma kinetics, we conclude that a finite anisotropy conveniently causes a preferred emission of light into the backwards half sphere as also indicated, e.g., in Ref. [51].

O'Shay *et al.* [56] estimated the total amount of radiated energy from a tin LPP in  $4\pi$  steradian to be on the order of 90% of the absorbed laser energy. Tillack *et al.* [57] simulated the energy balance of spherical tin targets and concluded that about 70% of the energy is converted into radiation. This is in broad agreement with the 70–80% estimate from the simulations presented in Ref. [55]. Combining our fit value with this approximately 80% theory value we conclude that approximately 30% of the laser light is converted into radiation emitted in the forward half sphere. The in-band emission anisotropy in Fig. 2 also evidences a slight preference for backward emission. These findings are further supported by Refs. [49] and [50]. Our CE results are consistent with those obtained in Ref. [49] taking into account the droplet and beam spot sizes used.

The expansion velocity obtained from the fit agrees well with those inferred from radiation hydrodynamic simulations [55]. In that work, a 46- $\mu\text{m}$ -diameter droplet was irradiated by a 115- $\mu\text{m}$  FWHM Gaussian Nd:YAG laser beam at an average intensity of  $1.3 \times 10^{11}$  W/cm<sup>2</sup>. A dominant, 80% fraction of the laser light is absorbed in the region close to but before the critical surface [26]. Lateral expansion speeds on the order of  $v \sim 1$   $\mu\text{m}/\text{ns}$  resulted from the simulations for densities approximately  $0.1\text{--}0.5n_c$ .

Using the global fit values for  $\eta_{\text{max}}$  and  $t_h$ , we next apply and fit our model to the laser-intensity dependency in Fig. 4(g). Again, an excellent agreement is found between model and experiment, obtaining the parameter values  $a = 0.69(5)$  and  $b = 0.8(1)$ . This near-linear dependence of  $v$  on  $I$  is in line with the simulation data underpinning Ref. [55]. We note that  $t_h$  may also depend on intensity but its contribution to the 15-ns pulse-duration case is marginal and completely removing  $t_h$  from Eq. (3), in fact, does not significantly change the obtained values for the expansion velocity parameters  $a, b$ .

In conclusion, we can describe the scaling of the radiative efficiency with all studied parameters by a model describing the increase of laser absorption with plasma expansion. Excellent overall agreement between model and experimental data are obtained. We note that in our current investigations the effective radius  $R_{\text{eff}} = R_0 + v\tau$  remained below the beam radius  $w$  corresponding to case (i) in Eq. (3). The finite ellipticity of the laser-beam spot is not expected to significantly influence the measurements as the plasma expansion does neither exceed minor nor major axis. Values above our experimental maximum of 35%, possibly nearing 50%, appear to be feasible. Thus, in order to obtain high CE, a set of parameters needs to be found where a high value for SP is achieved while optimizing the absorbed fraction of laser light, or radiative efficiency. Changing the beam size in the following section enables us to probe beyond model case (i) and maximize radiative efficiency.

## VI. INCREASING RADIATIVE EFFICIENCY

In order to increase the radiative efficiency, and with it CE, the laser-beam size is reduced to  $56\ \mu\text{m}$ . As before, the beam-to-droplet overlap is scanned by changing droplet size (Fig. 6). The laser intensity is set to an optimal  $1.4 \times 10^{11}\ \text{W}/\text{cm}^2$  for SP and the laser pulse duration to 15 ns. The spectra for the small-beam spot size in Fig. 6(a) show a small but significant broadening of the main emission feature on its long wavelength side with a corresponding systematic reduction of SP in Fig. 6(b). This may be related to an absence of heating of the outer plasma layers beyond  $56\ \mu\text{m}$ .

A considerable overall increase in CE is obtained for all droplet sizes. It monotonically rises with the droplet diameter reaching a record-high value of 3.2%. We note that the ever more slowly decreasing values for SP/2 and increasing CE appear to converge to a common value. This intriguing observation indicates that the limit  $\text{CE} \leq \text{SP}/2$ , strictly valid only for isotropic emission [54], may provide a good estimate for the maximally reachable CE value of the plasma source.

Over the entire range measured, the radiative efficiency is monotonically increasing and significantly higher than for the  $96\text{-}\mu\text{m}$  laser beam [see Fig. 6(c)]. Comparing the small-beam measurements to the model results of Sec. V, we plot Eq. (3) using the values for  $v$  and  $t_h$  as determined from the global fit in Fig. 4. We set the beam spot size to  $56\ \mu\text{m}$  leaving only  $\eta_{\text{rad}}$  as a free fit parameter. The model fit shown with the dashed-dotted line in Fig. 6(c) is in excellent agreement with the experimental data. The obtained value for  $\eta_{\text{max}} = 42(1)\%$  is slightly lower than before, although within systematic uncertainties of determining beam spot and droplet size. The regime probed by these small-beam measurement includes model cases (ii) and (iii) that are not reachable in Sec. V. In these cases, the laser beam does not directly heat the laterally expanding high-density plasma at radii  $R_{\text{eff}} > w$ , which may affect  $\eta_{\text{rad}}$  through differences in the energy partitioning between forward and backward emission, and plasma kinetics. Further, the finite ellipticity of the laser-beam spot may slightly influence the measurements as the plasma expansion in these cases (ii) and (iii) exceeds major and minor axis over the scanned parameter range.

Aside from the already explored reduction of laser-beam spot and increase of droplet size to improve  $\eta_{\text{rad}}$ , our model shows that laser pulses of even longer duration could also be employed to compensate for a geometrical mismatch. For all three solutions, increases in  $\eta_{\text{rad}}$  are partially offset by a decrease in SP. Given the limit conditions  $\text{CE} \leq \text{SP}$  or the apt  $\text{CE} \leq \text{SP}/2$ , any global approach to source optimization needs to maximize both SP and the laser-plasma overlap captured by  $\eta_{\text{rad}}$ . Based on these considerations and our spectroscopic measurements in Fig. 6(a) from which we obtain values for SP above 12%, conversion

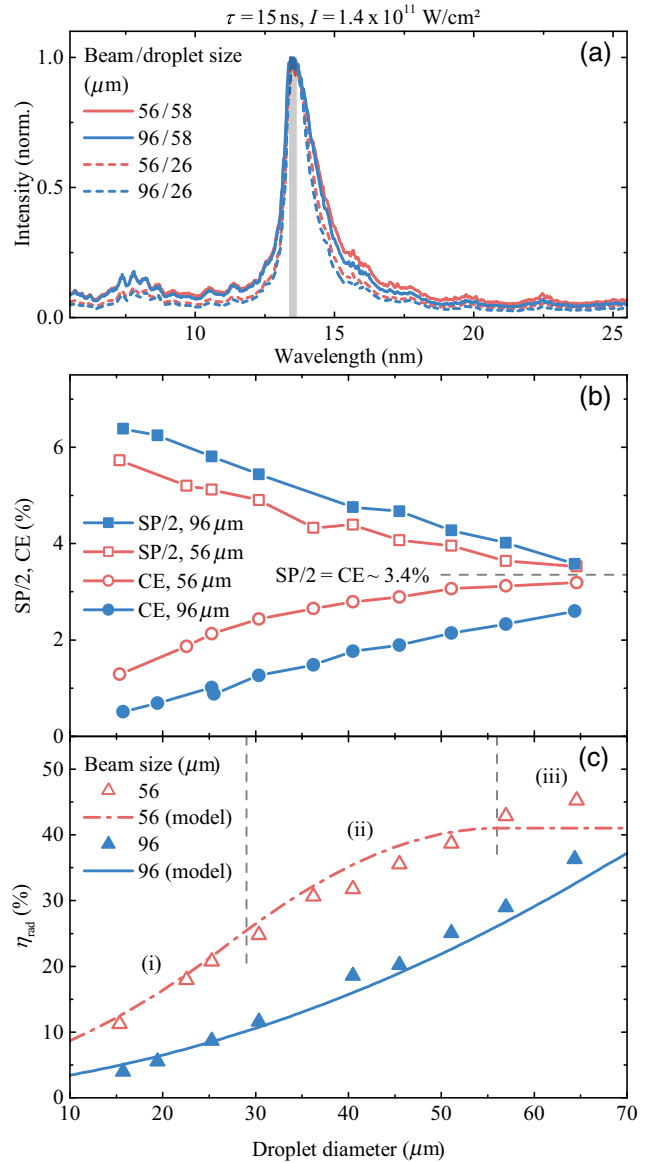


FIG. 6. (a) Spectra for two droplet sizes and two laser-beam sizes (see main text) at a laser intensity of  $1.4 \times 10^{11}\ \text{W}/\text{cm}^2$ ; (b) values for SP/2 and CE versus droplet diameter for the two laser-beam sizes; (c) radiative efficiency versus droplet diameter for the two laser-beam sizes. The dash-dotted and solid lines represent the model curves. For the  $56\text{-}\mu\text{m}$  laser beam, the regimes corresponding to the three model cases (i)–(iii) of Eq. (3) are highlighted by the vertical dashed lines (see main text).

efficiencies of  $\text{CE} = \text{SP}/2 = 6\%$  may in fact be achievable. These values would rival those of current  $\text{CO}_2$ -laser-driven sources. To obtain such efficiencies, the observed systematic decrease of SP with decreasing beam size needs to be negated. The model points towards another class of solutions including maximizing  $\eta_{\text{rad}}$  by using a separate laser “prepulse” to predeform the microdroplet into a disk shape [16–23] that closely matches the applied “main” laser-beam spot size.



## VII. CONCLUSION

We experimentally investigate the emission of EUV light from Nd:YAG laser-produced plasma over a wide parameter range, varying the laser energy, its pulse duration, and the size of the tin microdroplets. Spectroscopic measurements combined with absolute measurements of the emission into a 2% bandwidth around 13.5 nm allow us to obtain the scaling of three coupled parameters: the spectral purity SP, the conversion efficiency CE, and the radiative efficiency  $\eta_{\text{rad}}$  expressed as the ratio CE/SP. We successfully capture all observed scalings of  $\eta_{\text{rad}}$  in a geometrical model featuring the plasma absorption length as the pertinent parameter. Using a smaller laser-beam spot size, approaching the size of the droplets, we obtain a record-high 3.2% conversion efficiency of laser light into in-band radiation. Energy conservation considerations bind the maximum value of CE to SP/2 for isotropic emission, and our measurements strongly hint at the convergence of CE towards this theoretical limit. A 6% conversion efficiency value may thus be achievable in future experiments that should also quantify and compare the debris produced by Nd:YAG laser-produced plasma sources to industrial ones using CO<sub>2</sub> lasers. High values for the key parameter, the conversion efficiency, are indeed obtainable from a single 1- $\mu\text{m}$ -laser-pulse irradiation scheme. Combining these high conversion-efficiency values with the advantages of reduced footprint, beneficial wall-plug efficiency, and laser stability this work enhances the prospects that Nd:YAG-driven LPP light sources will find application in EUV nanolithography.

## ACKNOWLEDGMENTS

This work is carried out at the Advanced Research Center for Nanolithography (ARCNL), a public-private partnership of the University of Amsterdam (UvA), the Vrije Universiteit Amsterdam (VU), the Netherlands Organisation for Scientific Research (NWO), and the semiconductor equipment manufacturer ASML.

- [1] G. O'Sullivan, B. Li, R. D'Arcy, P. Dunne, P. Hayden, D. Kilbane, T. McCormack, H. Ohashi, F. O'Reilly, P. Sheridan, E. Sokell, C. Suzuki, and T. Higashiguchi, Spectroscopy of highly charged ions and its relevance to EUV and soft X-ray source development, *J. Phys. B: At. Mol. Opt. Phys.* **48**, 144025 (2015).
- [2] V. I. Azarov and Y. N. Joshi, Analysis of the  $4d^7-4d^6\ 5p$  transition array of the eighth spectrum of tin: Sn VIII, *J. Phys. B: At. Mol. Opt. Phys.* **26**, 3495 (1993).
- [3] W. Svendsen and G. O'Sullivan, Statistics and characteristics of xuv transition arrays from laser-produced plasmas of the elements tin through iodine, *Phys. Rev. A* **50**, 3710 (1994).
- [4] S. S. Churilov and A. N. Ryabtsev, Analyses of the Sn IX–Sn XII spectra in the EUV region, *Phys. Scr.* **73**, 614 (2006).
- [5] S. S. Churilov and A. N. Ryabtsev, Analysis of the  $4p^6\ 4d^7-(4p^6\ 4d^6\ 4f+4p^5\ 4d^8)$  transitions in the Sn VIII spectrum, *Opt. Spectrosc.* **100**, 660 (2006).
- [6] S. S. Churilov and A. N. Ryabtsev, Analysis of the spectra of In XII–XIV and Sn XIII–XV in the far-VUV region, *Opt. Spectrosc.* **101**, 169 (2006).
- [7] A. N. Ryabtsev, É. Y. Kononov, and S. S. Churilov, Spectra of rubidium-like Pd X–Sn XIV ions, *Opt. Spectrosc.* **105**, 844 (2008).
- [8] I. Y. Tolstikhina, S. S. Churilov, A. N. Ryabtsev, and K. N. Koshelev, in *EUV Sources for Lithography*, edited by V. Bakshi (SPIE Press, Bellingham, Washington, 2006) Chap. 4, p. 113.
- [9] R. D'Arcy, H. Ohashi, S. Suda, H. Tanuma, S. Fujioka, H. Nishimura, K. Nishihara, C. Suzuki, T. Kato, F. Koike, J. White, and G. O'Sullivan, Transitions and the effects of configuration interaction in the spectra of Sn XV–Sn XVIII, *Phys. Rev. A* **79**, 042509 (2009).
- [10] H. Ohashi, S. Suda, H. Tanuma, S. Fujioka, H. Nishimura, A. Sasaki, and K. Nishihara, EUV emission spectra in collisions of multiply charged Sn ions with He and Xe, *J. Phys. B: At. Mol. Opt. Phys.* **43**, 065204 (2010).
- [11] A. Windberger, F. Torretti, A. Borschevsky, A. Ryabtsev, S. Dobrodey, H. Bekker, E. Eliav, U. Kaldor, W. Ubachs, R. Hoekstra, J. R. Crespo López-Urrutia, and O. O. Versolato, Analysis of the fine structure of  $\text{Sn}^{11+}$ – $\text{Sn}^{14+}$  ions by optical spectroscopy in an electron-beam ion trap, *Phys. Rev. A* **94**, 012506 (2016).
- [12] J. Colgan, D. Kilcrease, J. Abdallah, M. Sherrill, C. Fontes, P. Hakel, and G. Armstrong, Atomic structure considerations for the low-temperature opacity of Sn, *High Energy Density Phys.* **23**, 133 (2017).
- [13] F. Torretti, A. Windberger, A. Ryabtsev, S. Dobrodey, H. Bekker, W. Ubachs, R. Hoekstra, E. V. Kahl, J. C. Berengut, J. R. C. López-Urrutia, and O. O. Versolato, Optical spectroscopy of complex open- $4d$ -shell ions  $\text{Sn}^{7+}$ – $\text{Sn}^{10+}$ , *Phys. Rev. A* **95**, 042503 (2017).
- [14] V. Y. Banine, K. N. Koshelev, and G. H. P. M. Swinkels, Physical processes in EUV sources for microlithography, *J. Phys. D: Appl. Phys.* **44**, 253001 (2011).
- [15] J. Benschop, V. Banine, S. Lok, and E. Loopstra, Extreme ultraviolet lithography: Status and prospects, *J. Vac. Sci. Technol. B* **26**, 2204 (2008).
- [16] Y. Kawasuji, K. M. Nowak, T. Hori, T. Okamoto, H. Tanaka, Y. Watanabe, T. Abe, T. Kodama, Y. Shiraishi, H. Nakarai *et al.*, in *SPIE Advanced Lithography*, Vol. 10143 (International Society for Optics and Photonics, San Jose, California, United States, 2017) p. 101432G.
- [17] I. Fomenkov, D. Brandt, A. Ershov, A. Schafgans, Y. Tao, G. Vaschenko, S. Rokitski, M. Kats, M. Vargas, M. Purvis *et al.*, Light sources for high-volume manufacturing EUV lithography: technology, performance, and power scaling, *Adv. Opt. Techn.* **6**, 173 (2017).
- [18] M. Purvis, I. V. Fomenkov, A. A. Schafgans, M. Vargas, S. Rich, Y. Tao, S. I. Rokitski, M. Mulder, E. Buurman, M. Kats *et al.*, in *Extreme Ultraviolet (EUV) Lithography IX*, Vol. 10583 (International Society for Optics and Photonics, 2018) p. 1058327.

- [19] D. Kurilovich, A. L. Klein, F. Torretti, A. Lassise, R. Hoekstra, W. Ubachs, H. Gelderblom, and O. O. Versolato, Plasma Propulsion of a Metallic Microdroplet and its Deformation upon Laser Impact, *Phys. Rev. Appl.* **6**, 014018 (2016).
- [20] D. Kurilovich, T. de Faria Pinto, F. Torretti, R. Schupp, J. Scheers, A. S. Stodolna, H. Gelderblom, K. S. Eikema, S. Witte, W. Ubachs, R. Hoekstra, and O. O. Versolato, Expansion Dynamics after Laser-Induced Cavitation in Liquid Tin Microdroplets, *Phys. Rev. Appl.* **10**, 054005 (2018).
- [21] M. S. Krivokorytov, A. Y. Vinokhodov, Y. V. Sidelnikov, V. M. Krivtsun, V. O. Kompanets, A. A. Lash, K. N. Koshelev, and V. V. Medvedev, Cavitation and spallation in liquid metal droplets produced by subpicosecond pulsed laser radiation, *Phys. Rev. E* **95**, 031101 (2017).
- [22] S. Y. Grigoryev, B. Lakatos, M. Krivokorytov, V. Zhakhovsky, S. Dyachkov, D. Ilitsky, K. Migdal, N. Inogamov, A. Y. Vinokhodov, V. Kompanets *et al.*, Expansion and Fragmentation of A Liquid-Metal Droplet By A Short Laser Pulse, *Phys. Rev. Appl.* **10**, 064009 (2018).
- [23] V. Bakshi, ed., *EUV Lithography*, 2nd ed., (SPIE Press, Bellingham, Washington, 2018).
- [24] S. Bajt, J. B. Alameda, T. W. Barbee, Jr., W. M. Clift, J. A. Folta, B. Kaufmann, and E. A. Spiller, Improved reflectance and stability of Mo-Si multilayers, *Opt. Eng.* **41**, 1797 (2002).
- [25] Q. Huang, V. Medvedev, R. van de Kruijs, A. Yakshin, E. Louis, and F. Bijkerk, Spectral tailoring of nanoscale EUV and soft X-ray multilayer optics, *Appl. Phys. Rev.* **4**, 011104 (2017).
- [26] M. M. Basko, V. G. Novikov, and A. S. Grushin, On the structure of quasi-stationary laser ablation fronts in strongly radiating plasmas, *Phys. Plasmas* **22**, 053111 (2015).
- [27] P. Mora, Theoretical model of absorption of laser light by a plasma, *Phys. Fluids* **25**, 1051 (1982).
- [28] T. W. Johnston and J. M. Dawson, Correct values for high-frequency power absorption by inverse bremsstrahlung in plasmas, *Phys. Fluids* **16**, 722 (1973).
- [29] S. Fujioka, H. Nishimura, K. Nishihara, A. Sasaki, A. Sunahara, T. Okuno, N. Ueda, T. Ando, Y. Tao, Y. Shimada, K. Hashimoto, M. Yamaura, K. Shigemori, M. Nakai, K. Nagai, T. Norimatsu, T. Nishikawa, N. Miyanaga, Y. Izawa, and K. Mima, Opacity Effect on Extreme Ultraviolet Radiation from Laser-Produced Tin Plasmas, *Phys. Rev. Lett.* **95**, 235004 (2005).
- [30] H. Tanaka, A. Matsumoto, K. Akinaga, A. Takahashi, and T. Okada, Comparative study on emission characteristics of extreme ultraviolet radiation from CO<sub>2</sub> and Nd:YAG laser-produced tin plasmas, *Appl. Phys. Lett.* **87**, 041503 (2005).
- [31] P. Hayden, A. Cummings, N. Murphy, G. O'Sullivan, P. Sheridan, J. White, and P. Dunne, 13.5 nm extreme ultraviolet emission from tin based laser produced plasma sources, *J. Appl. Phys.* **99**, 093302 (2006).
- [32] J. White, P. Dunne, P. Hayden, F. O'Reilly, and G. O'Sullivan, Optimizing 13.5 nm laser-produced tin plasma emission as a function of laser wavelength, *Appl. Phys. Lett.* **90**, 181502 (2007).
- [33] R. C. Spitzer, T. J. Orzechowski, D. W. Phillion, R. L. Kauffman, and C. Cerjan, Conversion efficiencies from laser-produced plasmas in the extreme ultraviolet regime, *J. Appl. Phys.* **79**, 2251 (1996).
- [34] T. Ando, S. Fujioka, H. Nishimura, N. Ueda, Y. Yasuda, K. Nagai, T. Norimatsu, M. Murakami, K. Nishihara, N. Miyanaga, Y. Izawa, K. Mima, and A. Sunahara, Optimum laser pulse duration for efficient extreme ultraviolet light generation from laser-produced tin plasmas, *Appl. Phys. Lett.* **89**, 151501 (2006).
- [35] Y. Tao, S. Harilal, M. Tillack, K. Sequoia, B. O'Shay, and F. Najmabadi, Effect of focal spot size on in-band 13.5 nm extreme ultraviolet emission from laser-produced Sn plasma, *Opt. Lett.* **31**, 2492 (2006).
- [36] S. A. George, W. T. Silfvast, K. Takenoshita, R. T. Bernath, C.-S. Koay, G. Shimkaveg, and M. C. Richardson, Comparative extreme ultraviolet emission measurements for lithium and tin laser plasmas, *Opt. Lett.* **32**, 997 (2007).
- [37] O. Morris, F. O'Reilly, P. Dunne, and P. Hayden, Angular emission and self-absorption studies of a tin laser produced plasma extreme ultraviolet source between 10 and 18 nm, *Appl. Phys. Lett.* **92**, 2006 (2008).
- [38] K. L. Sequoia, Ph.D. thesis, UC San Diego, 2009.
- [39] Y. Tao, Y. Ueno, S. Yuspeh, R. Burdt, M. Tillack, and F. Najmabadi, in *Extreme Ultraviolet (EUV) Lithography II*, Vol. 7969 (International Society for Optics and Photonics, San Jose, California, United States, 2011) p. 796930.
- [40] A. Roy, S. Murtaza Hassan, S. S. Harilal, A. Endo, T. Mocek, and A. Hassanein, Extreme ultraviolet emission and confinement of tin plasmas in the presence of a magnetic field, *Phys. Plasmas* **21**, 053106 (2014).
- [41] A. Roy, G. Arai, H. Hara, T. Higashiguchi, H. Ohashi, A. Sunahara, B. Li, P. Dunne, G. O'Sullivan, T. Miura *et al.*, Evolution of laser-produced Sn extreme ultraviolet source diameter for high-brightness source, *Appl. Phys. Lett.* **105**, 074103 (2014).
- [42] M. Su, Q. Min, S. Cao, D. Sun, P. Hayden, G. O'Sullivan, and C. Dong, Evolution analysis of EUV radiation from laser-produced tin plasmas based on a radiation hydrodynamics model, *Sci. Rep.* **7**, 45212 (2017).
- [43] S. Fujioka, H. Nishimura, K. Nishihara, M. Murakami, Y.-G. Kang, Q. Gu, K. Nagai, T. Norimatsu, N. Miyanaga, Y. Izawa *et al.*, Properties of ion debris emitted from laser-produced mass-limited tin plasmas for extreme ultraviolet light source applications, *Appl. Phys. Lett.* **87**, 241503 (2005).
- [44] Y. Shimada, H. Nishimura, M. Nakai, K. Hashimoto, M. Yamaura, Y. Tao, K. Shigemori, T. Okuno, K. Nishihara, T. Kawamura *et al.*, Characterization of extreme ultraviolet emission from laser-produced spherical tin plasma generated with multiple laser beams, *Appl. Phys. Lett.* **86**, 051501 (2005).
- [45] S. Yuspeh, K. Sequoia, Y. Tao, M. Tillack, R. Burdt, and F. Najmabadi, Optimization of the size ratio of Sn sphere and laser focal spot for an extreme ultraviolet light source, *Appl. Phys. Lett.* **93**, 221503 (2008).
- [46] S. Yuspeh, Y. Tao, R. Burdt, M. Tillack, Y. Ueno, and F. Najmabadi, Dynamics of laser-produced Sn microplasma for a high-brightness extreme ultraviolet light source, *Appl. Phys. Lett.* **98**, 201501 (2011).
- [47] J. Freeman, S. Harilal, B. Verhoff, A. Hassanein, and B. Rice, Laser wavelength dependence on angular emission dynamics of Nd:YAG laser-produced Sn plasmas, *Plasma Sources Sci. Technol.* **21**, 055003 (2012).

- [48] A. Y. Vinokhodov, M. S. Krivokorytov, Y. V. Sidelnikov, V. M. Krivtsun, V. V. Medvedev, and K. N. Koshelev, Droplet-based, high-brightness extreme ultraviolet laser plasma source for metrology, *J. Appl. Phys.* **120**, 163304 (2016).
- [49] A. Z. Giovannini and R. S. Abhari, Three-dimensional extreme ultraviolet emission from a droplet-based laser-produced plasma, *J. Appl. Phys.* **114**, 033303 (2013).
- [50] A. Z. Giovannini and R. S. Abhari, Effects of the dynamics of droplet-based laser-produced plasma on angular extreme ultraviolet emission profile, *Appl. Phys. Lett.* **104**, 194104 (2014).
- [51] H. Chen, X. Wang, L. Duan, H. Lan, Z. Chen, D. Zuo, and P. Lu, Angular distribution of ions and extreme ultraviolet emission in laser-produced tin droplet plasma, *J. Appl. Phys.* **117**, 193302 (2015).
- [52] S. Goh, H. Bastiaens, B. Vratzov, Q. Huang, F. Bijkerk, and K. Boller, Fabrication and characterization of free-standing, high-line-density transmission gratings for the vacuum UV to soft X-ray range, *Opt. Express* **23**, 4421 (2015).
- [53] M. Bayraktar, H. M. Bastiaens, C. Bruineman, B. Vratzov, and F. Bijkerk, Broadband transmission grating spectrometer for measuring the emission spectrum of EUV sources, *NEVAC Blad* **54**, 14 (2016).
- [54] M. Basko, On the maximum conversion efficiency into the 13.5-nm extreme ultraviolet emission under a steady-state laser ablation of tin microspheres, *Phys. Plasmas* **23**, 083114 (2016).
- [55] D. Kurilovich, M. M. Basko, D. A. Kim, F. Torretti, R. Schupp, J. C. Visschers, J. Scheers, R. Hoekstra, W. Ubachs, and O. O. Versolato, Power-law scaling of plasma pressure on laser-ablated tin microdroplets, *Phys. Plasmas* **25**, 012709 (2018).
- [56] B. O'Shay, F. Najmabadi, S. Harilal, and M. Tillack, in *Journal of Physics: Conference Series*, Vol. 59 (IOP Publishing, Banff, Canada, 2007) p. 773.
- [57] M. Tillack, K. Sequoia, and Y. Tao, in *Journal of Physics: Conference Series*, Vol. 112 (IOP Publishing, Kobe, Japan, 2008) p. 042060.
- [58] R. A. Meijer, A. S. Stodolna, K. S. E. Eikema, and S. Witte, High-energy Nd:YAG laser system with arbitrary sub-nanosecond pulse shaping capability, *Opt. Lett.* **42**, 2758 (2017).
- [59] A. Kramida, Y. Ralchenko, J. Reader, and NIST ASD Team, NIST Atomic Spectra Database (ver. 5.3), [Online]. Available: <http://physics.nist.gov/asd> [2016, February 2]. National Institute of Standards and Technology, Gaithersburg, MD. 2015.
- [60] M. Yamaura, S. Uchida, A. Sunahara, Y. Shimada, H. Nishimura, S. Fujioka, T. Okuno, K. Hashimoto, K. Nagai, T. Norimatsu *et al.*, Characterization of extreme ultraviolet emission using the fourth harmonic of a Nd:YAG laser, *Appl. Phys. Lett.* **86**, 181107 (2005).
- [61] F. Torretti, R. Schupp, D. Kurilovich, A. Bayerle, J. Scheers, W. Ubachs, R. Hoekstra, and O. Versolato, Short-wavelength out-of-band EUV emission from Sn laser-produced plasma, *J. Phys. B: At. Mol. Opt. Phys.* **51**, 045005 (2018).
- [62] C. R. Phipps, T. P. Turner, R. F. Harrison, G. W. York, W. Z. Osborne, G. K. Anderson, X. F. Corlis, L. C. Haynes, H. S. Steele, K. C. Spicochi, and T. R. King, Impulse coupling to targets in vacuum by KrF, HF, and CO<sub>2</sub> single-pulse lasers, *J. Appl. Phys.* **64**, 1083 (1988).
- [63] M. Murakami, J. Meyer-ter Vehn, and R. Ramis, Thermal X-ray emission from ion-beam-heated matter, *J. Xray Sci. Technol.* **2**, 127 (1990).
- [64] M. Murakami, S. Fujioka, H. Nishimura, T. Ando, N. Ueda, Y. Shimada, and M. Yamaura, Conversion efficiency of extreme ultraviolet radiation in laser-produced plasmas, *Phys. Plasmas* **13**, 033107 (2006).